AIAA JOURNAL
Vol. 45, No. 1, January 2007

Effects of Cylinder Wake on Separated Boundary Layer of a Wing

R. F. Huang* and J. S. Wu†
National Taiwan University of Science and Technology, Taipei 106, Taiwan, Republic of China

DOI: 10.2514/1.24517

The particle-tracking flow visualization method and the particle image velocimetry are employed to study the effects of a cylinder wake on the formation, evolution, and shedding processes of the vortical flow structures around the NACA 0012 wing. The experiments are conducted in a towing water tank. The wing is operated at the Reynolds number of 1200 and an angle of attack of 15 deg where the boundary layer on the suction surface is separated. A rigid metallic circular cylinder with a small diameter of 4 mm is placed at various positions near the leading edge of the wing with an offset distance from the chord axis to affect the vortical flows in the separated boundary layer on the suction surface and the vortex shedding in the wake of the wing. When the circular cylinder is placed in an appropriate region near the wing leading edge, a jetlike flow going through the gap between the circular cylinder and the wing surface could be formed. This jetlike flow acts like a high momentum "flow curtain" going across the separated boundary layer above the wing surface. Therefore, the thickness of the separated boundary layer is drastically decreased and the vortex shedding frequency (and also the Strouhal number) is significantly increased when compared with those of the natural wing.

Nomenclature

c	=	chord length of the wing model
d	=	length of wing section projection on cross-stream plane
f	=	vortex shedding frequency in wing wake
Re_c	=	Reynolds number based on chord length of wing ($Re_c = \bar{u}d/\nu$)
r	=	distance between point on chord line located at $8/c$ from wing leading edge and center of circular cylinder
Sr_d	=	Strouhl number of vortex shedding ($=fd/\bar{u}$)
s	=	span of wing
t	=	time of evolution after start of towing
t^*	=	reduced time ($=t\bar{u}/c$)
u	=	instantaneous velocity in ξ direction
$\bar{u}$	=	time-averaged towing velocity
v	=	instantaneous velocity in η direction
x	=	chordwise coordinate originated at leading edge of wing on root plane
y	=	cross-chordwise coordinate originated at leading edge of wing on root plane
z	=	spanwise coordinate originated at leading edge of wing on the root plane
α	=	angle of attack of wing
η	=	coordinate attached to view window of particle image velocimetry measurement, normal toξ
θ	=	angle between chord line and line connecting points on the chord line located at $c/8$ from wing leading edge and center of circular cylinder
ν	=	kinematic viscosity of water
ξ	=	coordinate attached to view window of particle image velocimetry measurement, pointing to towing direction
ϕ	=	diameter of circular cylinder

Received 8 April 2006; revision received 5 October 2006; accepted for publication 18 October 2006. Copyright © 2006 by the American Institute of Aeronautics and Astronautics, Inc. All rights reserved. Copies of this paper may be made for personal or internal use, on condition that the copier pay the $10.00 per-copy fee to the Copyright Clearance Center, Inc., 222 Rosewood Drive, Danvers, MA 01923; include the code $10.00 in correspondence with the CCC.

*Professor, Department of Mechanical Engineering. Senior Member AIAA.

†Graduate Student, Department of Mechanical Engineering.

Introduction

THE time-evolving vortical flow structures on a wing suction surface at low Reynolds numbers have been noticed by many investigators [1–6]. Ohmi et al. [3] studied the vortex formation process around a NACA 0012 airfoil. At low reduced oscillating frequencies, no substantial differences between the wakes of the static airfoil were found. Coutanceau and Pineau [4] reviewed the time-evolution process of vortical flow structures behind various bluff bodies. Nair and Sengupta [5] have calculated the unsteady flow past an elliptic cylinder by using numerical schemes. Huang et al. [6] presented streak pictures of the vortex evolution process on which the suction surface of a wing were obtained. They found that stable vortex shedding in the wake was eventually established after the initial period of complex vortex evolution process on the suction surface of the wing and was closely related to the evolution of the surface vortices. The complex boundary-layer behaviors of the wing at low Reynolds numbers are difficult to manage because the viscous force usually dominated in this regime. The turbulence generated by most of the effective flow control methods [7,8] commonly used in the mediate and high Reynolds number regimes is easily dissipated and would not ensure an effective control on the boundary layer and the wake instabilities. Therefore, the detailed flow behaviors and mechanisms of effective control on the flows around an airfoil in the viscous effect-dominated regime are hardly found in the literature because of the difficulty of dispersion of turbulent momentum.

Strykowski and Sreenivasan [9] reported that the vortex shedding of a circular cylinder at Reynolds numbers up to 80 can be dramatically suppressed by properly placing a small circular cylinder in the near-wake shear layer of the main cylinder. It was argued that the properly placed small cylinder weakens the shear layer by spreading the velocity gradient (i.e., diffusing vorticity) over a large distance. When the small cylinder was placed farther outside but near to the locus of maximum vorticity, the wake of the small cylinder was most effective in reducing the circulation in that portion of the shear layer which was most critical for vortex formation. If the circulation was reduced below some threshold level in the formation region, the mutual attraction between the opposing shear layers would be too weak to form the vortex roll-ups.

Although the small cylinder method is effective for the management of the boundary layer around a main cylinder as mentioned before [9], it does not assure the effectiveness in the case of an airfoil because the boundary-layer behaviors of the airfoil are not the same as those of a cylinder [6]. The objectives of this study are focused on studying the effect of a cylinder wake on the separated

boundary layer and the vortex shedding of an NACA 0012 wing in the regime of low Reynolds numbers. The wing is set at an angle of attack of 15 deg where the boundary layer on the suction surface is separated [1,2,6]. The surface flow and the vortex shedding in the wake are managed by placing a circular cylinder at a distance above the suction surface around the leading edge of the wing. Both the evolution processes of the large structures on the suction surface of the wing, started from rest with and without effects of cylinder wake, are presented and discussed. The velocity and vorticity distributions, the boundary-layer thickness, and the vortex shedding frequency characteristics of the cylinder-wake affected wing are studied and compared with those of the natural wing.

Experiments

Experimental Apparatus

The experiments are conducted in a transparent, open-top, rectangular water tank. The water tank is 60 cm wide, 60 cm deep, and 210 cm long, with a closed-loop towing mechanism surrounded, as shown in Fig. 1. A moving block, which serves as an object carrier, is sited on two cautiously calibrated parallel stainless rails. The stainless rails are in turn mounted on a steel chassis over the top of the water tank. The moving block is dragged by a metallic sprocket chain, which is driven by an ac servomotor. The motion of the servomotor is controlled by a PC-based feedback controller. The moving block can attain a stable target speed from rest within about 0.24 s. In terms of the reduced time, it is within about 0.028.

A NACA 0012 wing model [10] made of aluminum alloy is mounted under the moving block. The wing model has a chord length of 6 cm and a span of 30 cm, so that the aspect ratio is five. The surface of the wing model is anodized black to avoid scattering of the laser light. A circular cylinder made of stainless steel with a diameter of 4 mm is installed around the leading-edge area of the wing and parallel to the wing span, as shown in Fig. 2. The circular cylinder is fastened to the wing through a specially designed miniature connecting mechanism. The cylinder can be positioned freely around the wing nose area. In this paper, experimental results at $\theta = 20, 45,$ and 60 deg are presented. The normalized radius r/c is set to 0.167.

The coordinate system adopted is shown at the lower left corner of Fig. 1. A set of coordinates (ξ, η) is also employed to locate the viewing window of the particle image velocimetry (PIV) measurements. The charge-coupled device (CCD) camera or the static camera is mounted (facing the z direction) on the bottom of a steel frame, so that the camera can move sturdily with the motion of the moving block and the image frame can always aim at the same viewing window.

Flow Visualization

In performing the particle-tracking flow visualization, plastic particles made of polyamide are seeded in the water tank to scatter the laser light. The diameters of particles are between 30 and 70 μm and the specific weight is 1.03 at 25°C. Ignoring the effect of turbulent diffusion, the relaxation time constant is estimated to be less than 6.25×10^{-5} s and the Stokes number is in the order of 10^{-5} within the range of experiment. Therefore, the slip between the flow and particles can be neglected [11]. The laser beam issued from an argon-ion laser is transmitted through an optical fiber and then connected to a 20 deg laser-light sheet expander. The whole mechanism is designed so that the camera, wing model, and laser-light sheet can move simultaneously.

A film camera is used to take the long-exposure streak pictures. The exposure time is set at 0.5 s, so that apparent path lines of the particles can be recorded on the films. The path lines of the particle images are recorded on the streak films with long exposure time and low framing rate. The continuous motion images are also recorded and stored in the computer memories by using a CCD camera. Identification and analysis of formation and evolution processes of the vortex system on the suction surface are conducted either by replaying the movies of the particle images on a computer monitor or by tracing the long-exposure streak pictures.

PIV Measurements

In conducting the PIV measurements, a Redlake MotionScope PCI 2000S CCD camera is employed to record the particle images. During the experiment, the shutter speed and the framing rate are set

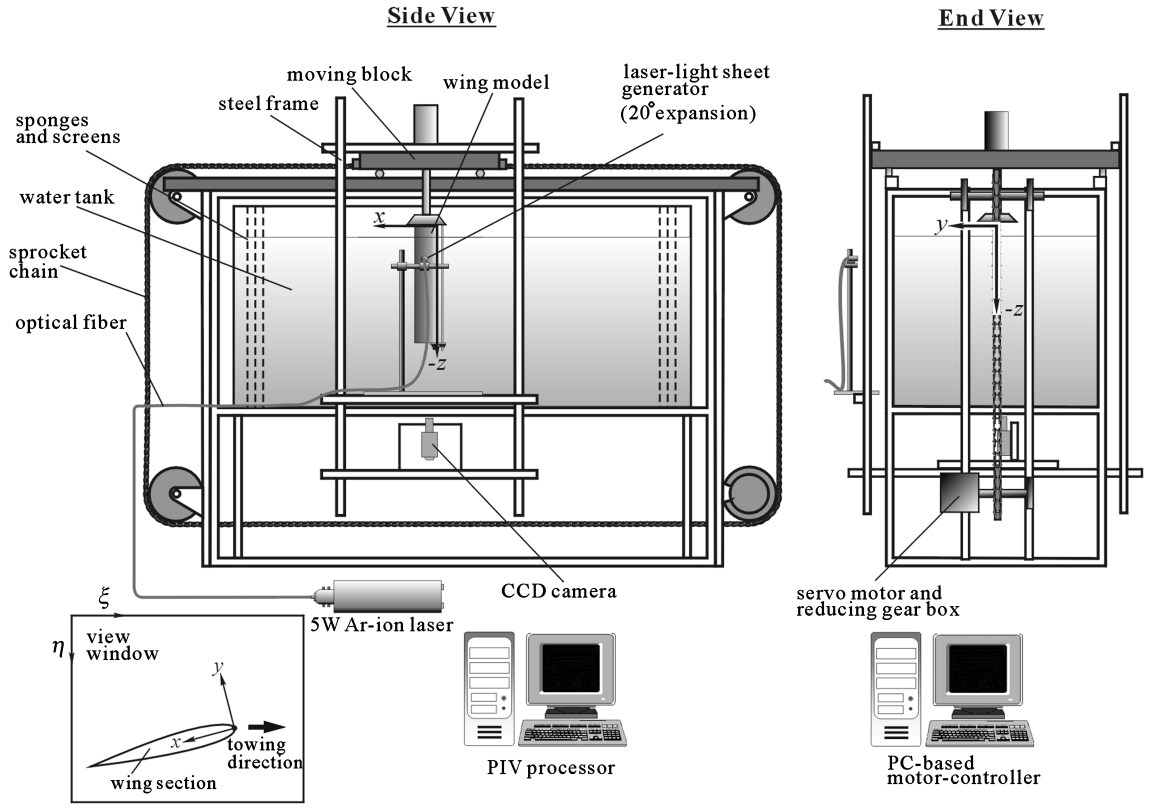

Fig. 1 Experimental setup.

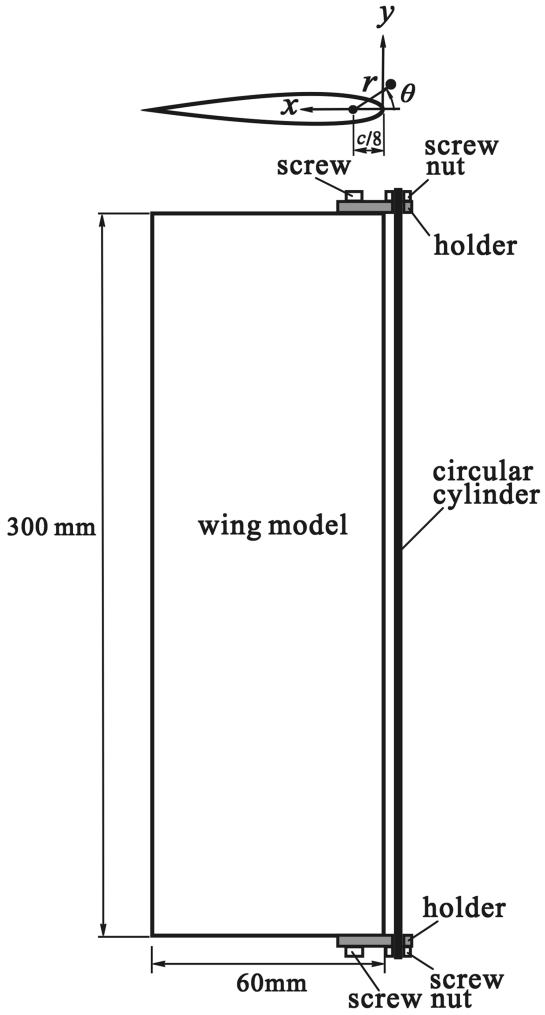

Fig. 2 Clamping and positioning mechanism of circular cylinder.

at 1/250 s and 60 frames/s, respectively. The separation time between consecutive pictures is thus 16.67 ms. Light-sensing array of the CCD camera is 480×420 pixels. Mapping to the physical domain of the view window of 80×70 mm, the spatial resolution thus is about 0.167×0.167 mm/pixel. Although the spatial resolution is not very high when compared with those typically used in the turbulent flow (smaller than 0.1×0.1 mm/pixel), it is enough to obtain continuous, acceptable data because the Reynolds number ($Re_c = 1200$) in these studies is relatively low. Therefore, smoothing is unnecessary. With these arrangements, the freestream particles would move about four pixels between two consecutive pictures at $Re_c = 1200$. Two consecutive image frames are analyzed by using the cross-correlation technique [12,13]. The software calculates the average displacement of local groups of particles in consecutive images. The interrogation window is set to 16×16 or 32×32 pixels.

A filter is used to discriminate outliers from valid vector values by comparing how close each vector component is to the mean of the vector values across the whole vector-map. In general, less than 5% of spurious vectors per instantaneous field are obtained in this study. The removed outliers are interpolated by a general-purpose interpolation kernel, which uses nearest 8 or 24 neighbor values for processing. The method of interpolation is based on a weighted mean technique which replaces the values at filtered sites in an iterative manner by replacing those with the most surrounding valid values first, then working toward those that are less favorably positioned for accurate and reliable interpolation.

The water in the tank is settled for at least five hours between two consecutive runs and can be taken as almost "draft-free" from the macroscopic point of view. Besides, because the Reynolds number is very low, the velocity data measured at the same instant of each run do not show variation over 0.6%. Therefore, the presented velocity vector maps and time-evolving streamline patterns are all simultaneous. They are not obtained by ensemble average of multiple-run data.

Uncertainties

The uncertainty estimates for each variable in the graphs are based on the method of Abernethy et al. [14]. The total uncertainty E of the variables can be found by combining systematic and random errors as $E = [B^2 + (tS_D)^2]^{1/2}$, where B is the systematic uncertainty, S_D is the standard deviation of the mean, and the degree of freedom t is determined to be two for a 95 confidence level. The systematic uncertainty B is estimated based on the calibration data and previous test experience, and the standard deviation of the mean S_D is computed from the raw measurement data. The accuracy of the velocity of the towing motion calibrated by using an optical rule is within $\pm 1.1\%$. The uncertainty of velocity measurements by considering the spatial resolution of light-sensing array of the camera, timing jittering of the synchronizer, and multiple-run variations is estimated to be about $\pm 1\%$. The uncertainty of the normalized velocity is within $\pm 2\%$. The frequency of vortex shedding is obtained by counting the vortex release rate observed on the recorded flow visualization streak pictures. The uncertainty of frequency measurement is estimated to be about $\pm 2.3\%$. The uncertainty of Strouhal number is within $\pm 4\%$.

Results and Discussion

Evolution of Vortices on Suction Surface

Natural Wing

The PIV measured velocity vectors and streamline patterns of the natural wing in the *separation vortex* regime at $\alpha = 15$ deg and $Re_c = 1200$ are shown in Fig. 3. The sequence of vortex motion describes detailed flow evolution process. At $t^* = 0.167$, a starting vortex accompanying with a saddle point [15] is observed near the trailing edge. A calm period comes after the trailing-edge starting vortex convected downstream. No specific vortical structure appears on the wing surface, as typically shown in the plot of $t^* = 0.667$.

At $t^* = 1.333$, a counterclockwise-rotating vortex is found on about one-third chord length of the wing suction surface. By examining the animation of the particle image frames, it is found that the elapsed time for inception of the vortex formation is at about

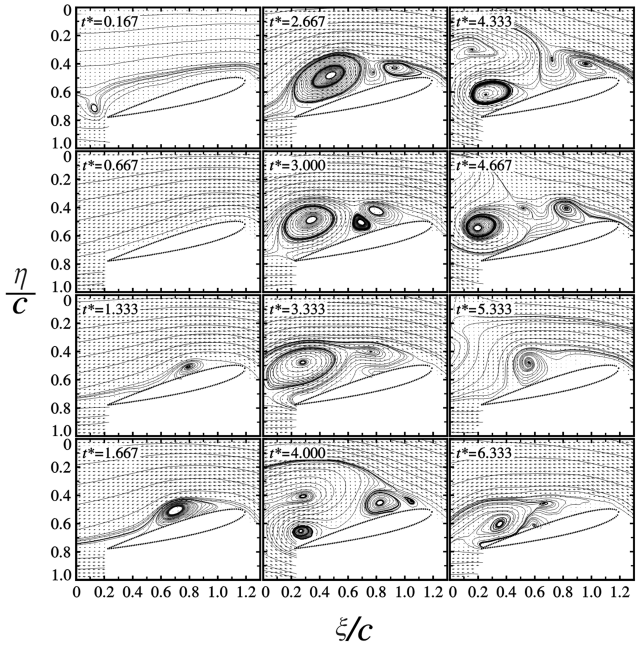

Fig. 3 Temporal and spatial evolution of streamlines on suction surface of natural wing.

$t^* = 1$. This initial vortex grows and rolls downstream as the time evolves, as shown in the plot of $t^* = 1.667$. At $t^* = 2.667$, two counter-rotating vortices appear on the suction surface downstream the leading edge and upstream the initial surface vortex. A four-way saddle must exist between the initial surface vortex and the leading-edge vortex pair. The initial surface vortex keeps going downstream and growing as the time evolves, as shown in the plot of $t^* = 3.0$. A saddle point appears at the lower left corner of the initial surface vortex because the stream coming from the lower surface of the wing has to merge with the counterflow of the initial surface vortex.

When the growing, counterclockwise-rotating initial surface vortex is about to leave the wing, the saddle point moves downstream, and the reverse flow induces the flow from the pressure surface to wrap around the trailing edge, as shown in the plot of $t^* = 3.333$. Simultaneously, the leading-edge vortex pair on the suction surface deforms due to the growth and convection of the initial surface vortex: the clockwise-rotating one is suppressed to the area near the wing suction surface and rolled over by the counterclockwise-rotating one. The four-way saddle now becomes a critical point which separates the counterclockwise-rotating initial surface vortex and the counterclockwise-rotating one of the leading-edge vortex pair. At $t^* = 4.000$, the initial vortex escapes from the view window, the counterclockwise-rotating one of the leading-edge vortex pair and the trailing-edge vortex which is induced by the reverse flow of the initial surface vortex enlarge, and a new pair of leading-edge vortices appears. At $t^* = 4.333$, the counterclockwise-rotating one of the initial leading-edge vortex pair proceeds to escape, the trailing-edge vortex and the new leading-edge vortex pair grow in size. At $t^* = 4.667$, one of the new leading-edge vortex pair (the clockwise-rotating one) evolves to become smaller in size and located in between the clockwise-rotating trailing-edge vortex and the new counterclockwise-rotating leading-edge vortex. Two four-way saddles can be identified at the upper-left and the lower-right regions of the clockwise-rotating vortex. These two saddle points must exist to satisfy the topological rule [15].

At $t^* = 5.333$, the trailing-edge vortex leaves the wing, the clockwise-rotating vortex disappears, and only the counterclockwise-rotating leading-edge vortex remains. This vortex rolls along the wing suction surface, then escapes to the wake. Afterward, a counterclockwise-rotating vortex is initiated on the wing suction surface, which is similar to the situation of $t^* = 1.333$. The subsequent vortical flow motions evolving on the suction surface of the wing follow the way similar to the initial period as described earlier and become periodic. For example, the plot at $t^* = 6.333$ shows the instantaneous flow pattern which is similar to that in the plot of $t^* = 3.333$. The evolution process repeats and becomes periodical. Along with the complex evolution process of the surface vortices, a stable vortex street, in which the surface vortex and the trailing-edge vortex shed alternatively to the downstream wake, is established.

Cylinder-Wake Affected Wing

Figure 4 shows the streak pictures obtained by the particle-tracking flow visualization method at $(Re_c, \alpha) = (1200, 15\,\text{deg})$ when a circular cylinder of $\phi/c = 0.066$ is installed at $(r/c, \theta) = (0.167, 20\,\text{deg})$. According to Roshko [16], in most of

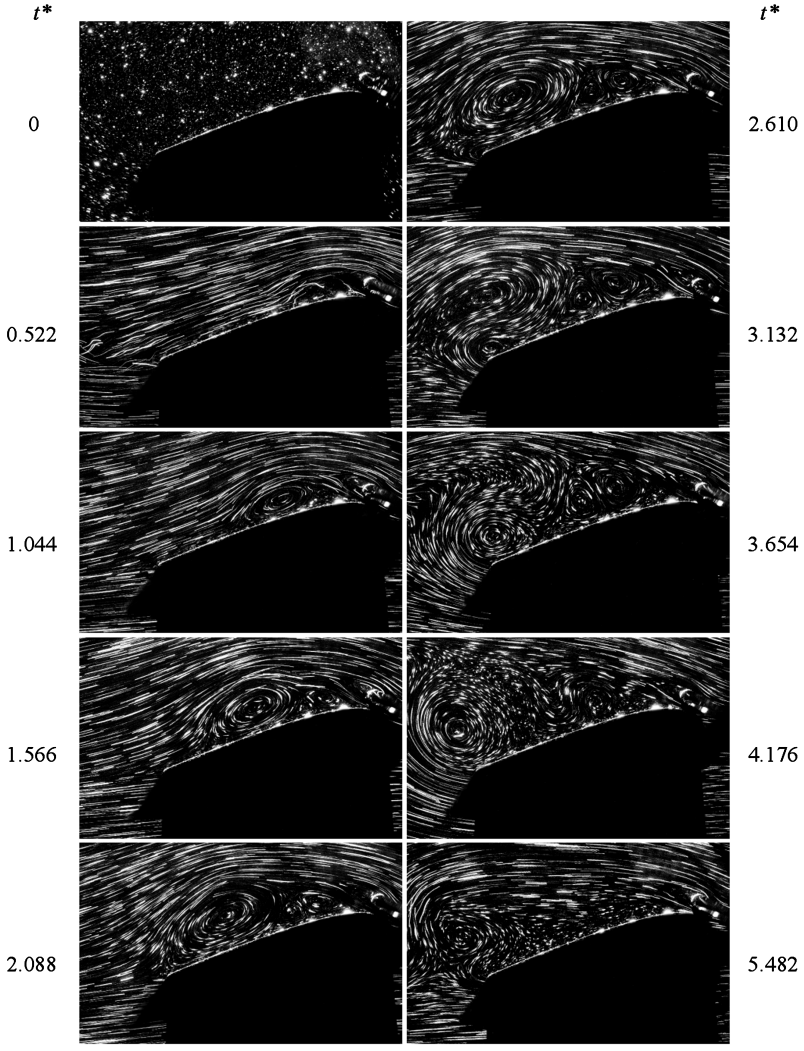

Fig. 4 Streak pictures of path lines of polyamide particles on suction surface of cylinder-wake affected wing.

the normal cases a pair of standing vortices would appear in the cylinder wake when the Reynolds number is in the range of $5 \sim 15 < Re_\phi < 45$. For $Re_\phi > 45$, vortex shedding would evolve in the wake. With the present arrangement, the Reynolds number based on the cylinder diameter is $Re_\phi = 80$, which is larger than the critical value of inducing vortex shedding in the cylinder wake. However, no trace of vortex shedding is found in the wake of the circular cylinder in Fig. 4. At $t^* = 0.522$, an initial surface vortex is formed on the suction surface within the upstream half of the chord length. Compared with the value $t^* \approx 1$ for the appearance of the first single vortex observed in the case of natural wing, the time elapsed as the first vortex is generated on the suction surface after the inception of towing is drastically shortened by about half. Besides, the location of initiating the first surface vortex is advanced to the upstream half of the suction surface (it is located around the midchord in the case of natural wing). The initial vortex formed on the suction surface rolls downstream along the suction surface and grows, as shown in the plot of $t^* = 1.044$. At $t^* = 1.566$ and 2.088, a counter-rotating leading-edge vortex pair, which is similar to that observed in the case of natural wing, is formed upstream the initial surface vortex. At $t^* = 2.610$ and 3.132, a flow structure, which evolves from the trailing edge of the pressure surface and wraps around to the suction surface to become a clockwise-rotating vortex, is induced because of the reverse flow of the initial surface vortex. From $t^* = 3.654$ to 4.176, the initial surface vortex escapes from the trailing edge of the wing and the induced trailing-edge vortex grows. At $t^* = 5.482$, the clockwise-rotating trailing-edge vortex is about to leave the wing trailing edge. The circular cylinder placed at the present location seems not to alter the evolution process of the vortical flows on the suction surface of the natural wing except the timing and the location of the formations of vortices.

The instantaneous streamline patterns, which are measured by the PIV at consecutive instants shown in Fig. 5, delineate clearly the evolution process, particularly the evolution process of the leading-edge vortex pair when the circular cylinder is installed at $(r/c, \theta) = (0.167, 20\,\text{deg})$. Figure 5 shows streak pictures of the path line images of particles on the suction surface of the cylinder-wake affected wing at $\alpha = 15\,\text{deg}$ and $Re_c = 1200$. No vortex shedding is observed in the cylinder wake. A calm period, as shown at $t^* = 0.278$, exists before any vortex is formed on the suction surface. At $t^* = 0.534$ and 0.835, a single vortex of counter-clockwise rotation is initiated and evolved. At $t^* = 1.286$, a new vortex is found in the upstream region of the initial surface vortex.

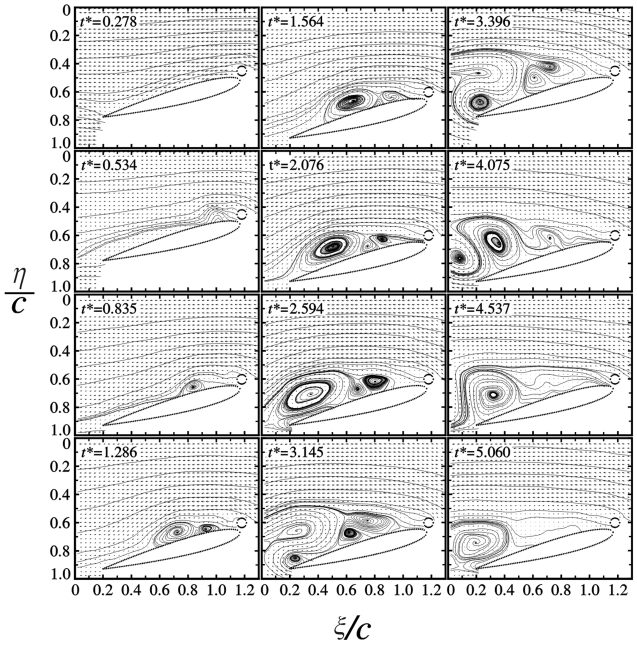

Fig. 5 Temporal and spatial evolution of streamlines on suction surface of cylinder-wake affected wing.

These two vortices have the same direction of counterclockwise rotation. Therefore, a four-way saddle must exist in between the initial surface vortex and the new vortex. The fluids enclosed in the small region beneath the four-way saddle, above the suction surface, and in between the initial surface vortex and the new vortex should possess momentum of clockwise rotation, owing to the flow topology [15]. The fluids in that small region then develop to form a clockwise-rotating vortex, as clearly seen in the plots of $t^* = 1.286$, 1.564, and 2.076. This clockwise-rotating vortex and the counterclockwise-rotating new vortex combine to form a counter-rotating leading-edge vortex pair with a vertex at a four-way saddle. The subsequent evolution process of the vortical flow on the suction surface of the cylinder-wake affected wing from $t^* = 2.076$ to 5.060 is similar to that of the natural wing. After going downstream of the counter-rotating vortex at $t^* = 5.060$, the evolution process goes back to the situation similar to that at $t^* = 0.534$: a surface vortex around the upstream half of the suction surface is initiated. Compared with the vortex evolution process on the natural wing shown in Fig. 3, apparently, the whole vortex evolution process on the suction surface of the cylinder-wake affected wing with $\theta = 20\,\text{deg}$ does not change in inherent characteristics. The existence of the circular cylinder and the flow going through the gap between the cylinder and the wing nose seems not to have substantial effect in altering the vortex evolution process on the wing surface. The stream momentum going through the gap between the circular cylinder and the wing nose is so small that the separation point on the suction surface is deferred downstream rather than the leading edge when comparison is made between Figs. 3 and 5.

However, as the circular cylinder is installed at $\theta = 45$ and 60 deg, the flow evolution process is drastically altered. Figure 6 shows streak pictures of the path line images of particles on the suction surface of the cylinder-wake affected wing at $\alpha = 15\,\text{deg}$ and $Re_c = 1200$. The cylinder with a diameter $\phi/c = 0.066$ is installed at $r/c = 0.167$ and $\theta = 60\,\text{deg}$. Under this situation, traces of characteristic flow structure just behind the cylinder are observable, although they are unclear and difficult to identify. Vague traces of the coherent flow structure can be observed just behind the cylinder. The flow structure induced in the near wake of the cylinder seems to be closely related to the flow going through the gap between the cylinder and the wing surface. Besides, wavy streams with appreciably large amplitudes present in the downstream wake of the circular cylinder. The fluids with large momentum (compared with those shown in Figs. 4 and 5 for the case of cylinder angle $\theta = 20$ deg) go through the gap between the cylinder and the wing surface and form a jetlike stream which goes across the separated boundary layer on the suction surface of the wing. This jetlike stream goes from the right to the left which is almost parallel to the axis of zero angle of attack (the ξ-axis) and becomes, in some sense, a flow curtain to "confine" upward growth of the separated boundary layer. The thickness (the height) of the separated boundary layer seems to be much smaller than that of the natural wing. The whole evolution of the vortical flow structures in the boundary layer occurs between the flow curtain and the suction surface of the wing. The flow going through the gap between the cylinder and the wing nose in the case of $\theta = 20\,\text{deg}$ is small, as shown in Figs. 4 and 5, due to the direction of the gap opening and the size of the gap. Therefore, the momentum "leakage" through the gap in the case of $\theta = 20\,\text{deg}$ is not large enough to form a jetlike stream to flush all the way across the wing suction surface. The flow evolution in that case, therefore, is not substantially modified when compared with that of the natural wing. However, in the case of Fig. 6 for the cylinder angle $\theta = 60\,\text{deg}$, the evolution process of the vortical flow structures in the separated boundary layer is drastically altered. At $t^* = 0.522$, 0.783, and 1.305, a counterclockwise-rotating surface vortex initiates at around the midchord and rolls downstream along the wing suction surface. Obviously, the initiation of the surface vortex is advanced in both the elapse time and the chordwise location when compared with those of the natural wing shown in Fig. 3. This is partially because of the enhanced shear effect induced by the strong gap flow. As the initial surface vortex rolls downstream to the area around the trailing edge, as shown in the picture of $t^* = 2.088$, a trailing-edge vortex is about to wrap from the

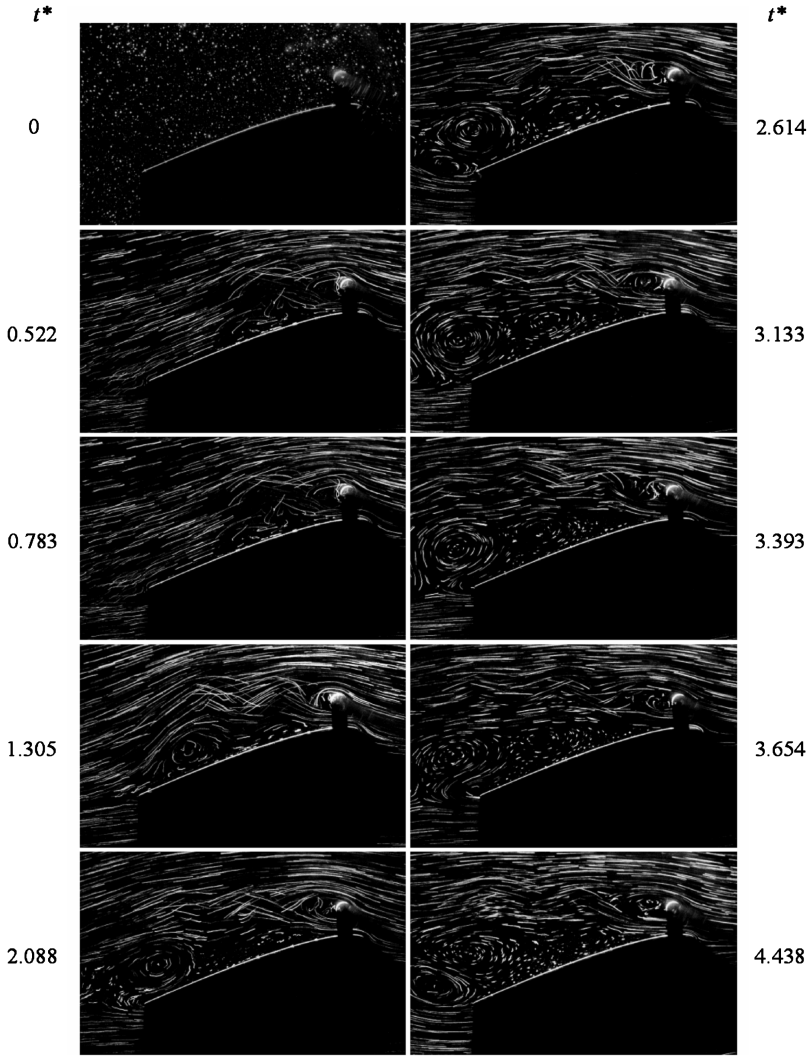

Fig. 6 Streak pictures of path lines of polyamide particles on suction surface of cylinder-wake affected wing.

pressure surface to the suction surface. At $t^* = 2.614$, the clockwise-rotating trailing-edge vortex grows, but does not roll upstream to the suction surface. Simultaneously, a new vortex upstream the initial surface vortex becomes clear. The initiation of the new surface vortex can be traced back to the pictures at $t^* = 1.305$ and 2.088. At $t^* = 3.133$, the trailing-edge vortex escapes out of the view window to the downstream wake. At $t^* = 3.393$, the initial surface vortex is about to escape and a new trailing-edge vortex is initiating. At $t^* = 3.654$ and 4.438, the trailing-edge vortex grows and is ready to shed. The new surface vortex, which becomes clearly observable upstream the initial surface vortex at $t^* = 2.614$, would shed successively after the escape of the trailing-edge vortex. The global evolution process seems to be concise. However, the details of the evolving vortical flow structures are still unclear.

The PIV measured velocity vectors and streamline patterns of the cylinder-wake affected wing at $\alpha = 15\,\text{deg}$, $Re_c = 1200$, and cylinder angle $\theta = 60\,\text{deg}$ are shown in Fig. 7. At $t^* = 0.328$, a starting vortex is observed near the wing trailing edge. In a calm period without any vortical flow structure evolving on the wing surface, as shown at $t^* = 0.679$, a vortex is initiating. The initial surface vortex rolls downstream along the wing surface to the trailing edge, as shown in the plots of $t^* = 1.041$, 1.369, and 1.620. At $t^* = 1.937$, the initial vortex splits into two counterclockwise-rotating vortices with a four-way saddle located in between. The downstream part of the initial surface vortex leaves for the wake and the upstream part remains. Simultaneously, a second surface vortex with the same rotation direction as the initial one is formed in the upstream area of the initial vortex one due to the interaction between

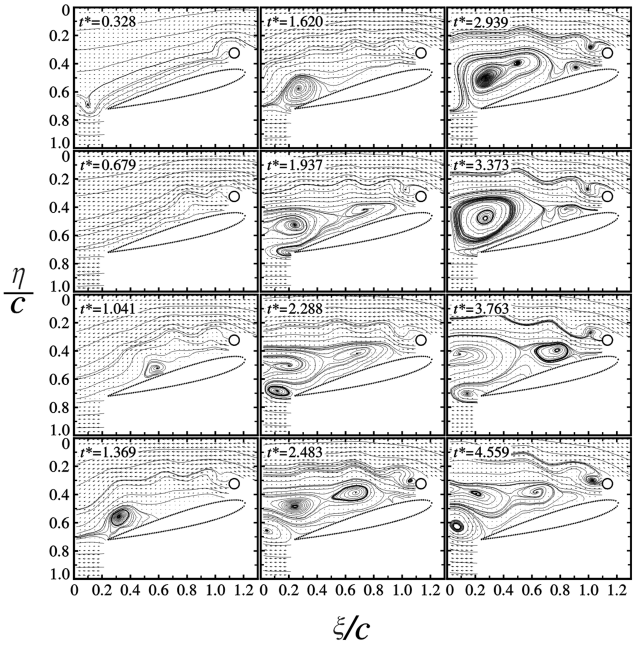

Fig. 7 Temporal and spatial evolution of streamlines on suction surface of cylinder-wake affected wing.

the cylinder wake and the first surface vortex. There is a saddle point existing between these two surface vortices to meet requirements of the topological rule. Also, a trailing-edge vortex appears. The trailing-edge vortex grows and escapes, as shown in the plots of $t^* = 2.288$ and 2.483. After the trailing-edge vortex escapes, a leading-edge vortex initiates upstream the clockwise-rotating surface vortex pair which occupies the major part of the suction surface, as shown in the plot of $t^* = 2.483$ and 2.939. At $t^* = 3.373$, the initial and the second surface vortices merge together to form a large single vortex and simultaneously, a trailing-edge vortex starts to establish. At $t^* = 3.763$, the merged large surface vortex rolls downstream and is about to escape. Both the induced trailing-edge vortex and the leading-edge vortex grow in size. The flow pattern at $t^* = 3.763$ becomes similar to that at $t^* = 1.937$. The surface vortex formation and vortex shedding processes then repeat successively. The evolution processes of the surface flows and the vortex shedding under the influence of the cylinder at $\theta = 60$ deg are apparently different from those of the natural wing and the cylinder-wake affected case at $\theta = 20$ deg.

The vague traces of the coherent flow structures observed just behind the circular cylinder in Fig. 6 can be identified in Fig. 7. It is a small vortex in the near wake of the cylinder, as shown in Fig. 7 for $t^* > 1.937$. When the flow passes over the circular cylinder, asymmetric flow property is induced because the wing model is located at the lower side of the cylinder. A small vortex along with a four-way saddle appears behind the wake of the cylinder. The small vortex and the four-way saddle toggle in the rotation directions as the time evolves. For instance, at $t^* = 3.373$, the small vortex behind the circular cylinder rotates in the clockwise direction and the four-way saddle is located above it. Whereas at $t^* = 3.763$, the rotation direction of the small vortex is reversed and the four-way saddle is located beneath it. The small vortex toggling alternatively in the upper and lower near wakes of the cylinder can be attributed to the periodic formation of the surface vortex on the suction surface of the wing. The periodic generation of the leading-edge surface vortex changes the state of the jet flow through the gap, and thus induces the toggling of the small vortex behind the cylinder wake. The toggling motion of the small vortex induces a wavy wake, instead of vortex shedding, in the downstream area of the cylinder. The wave motions of the cylinder wake have appreciably large amplitudes of oscillations. In between the wavy cylinder wake and the surface vortical flow structures there exists a layer of jetlike stream which is formed when the upstream flow penetrates through the gap between the cylinder and the wing. The whole evolution process that occurred in the separated boundary layer is restricted under this jetlike stream and the wavy cylinder wake.

The major differences of the typical flow structures of the separated boundary layers of the natural and the cylinder-wake affected wings can be examined using Figs. 8 and 9. In Fig. 8a, the wing is not affected by the cylinder. The flow pattern composed of the path lines of polyamide particles show clearly the trailing-edge vortex and the escaping primary surface vortex. However, the path lines of the particles in the leading-edge vortex pair are too short to trace so that the flow structures are unclear. The PIV measured velocity vectors and corresponding streamlines shown in Fig. 9a present the flow pattern at the time instance close to that of Fig. 8a. The velocity vectors in the region of the leading-edge vortex pair are relatively small compared with those in the other regions. The upper boundary of the primary surface vortex attains a level almost higher than 0.7 chord length. The vortical flow structures in the separated boundary layer of Fig. 8b for the cylinder-wake affected wing at $r/c = 0.167$, $\theta = 60$ deg at $t^* = 2.614$ are identifiable. However, the flow structure in the cylinder wake is difficult to describe. The PIV measured velocity vectors and corresponding streamlines shown in Fig. 9b delineate clearly the flow pattern at the time instance close to that of Fig. 8b. The separated boundary layer containing the vortical flow structures is drastically suppressed to the space under the jetlike wavy stream induced by the interaction between the gap flow and the cylinder wake.

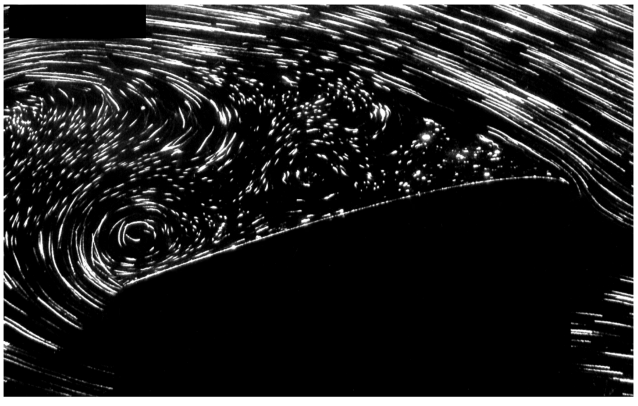

a) t^* = 4.436, natural wing

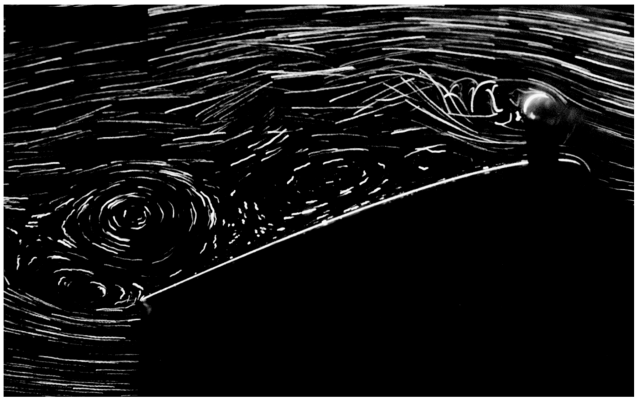

b) t^* = 2.614, cylinder-wake affected wing

Fig. 8 Comparison of path lines of polyamide particles on suction surface; $Re_c = 1200$, $\alpha = 15$ deg.

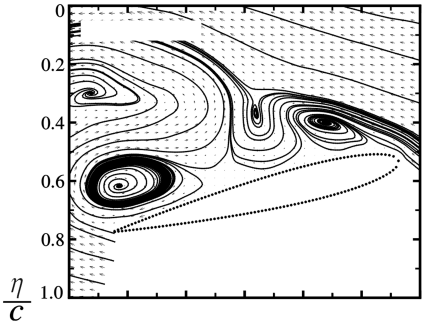

a) t^* = 4.333, natural wing

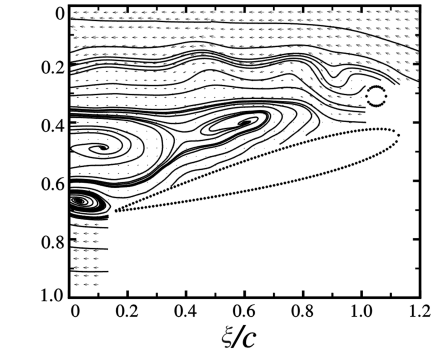

b) t^* = 2.288, cylinder-wake affected wing

Fig. 9 Comparison of streamlines on suction surface; $Re_c = 1200$, $\alpha = 15$ deg.

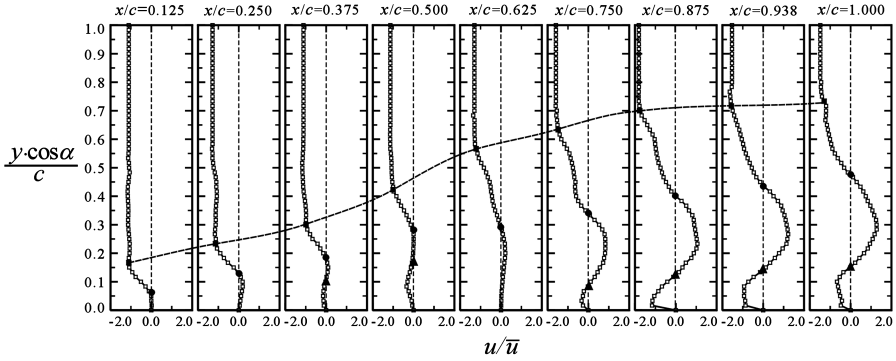

Fig. 10 Velocity distributions of normalized u-component on suction surface of natural wing.

Velocity Distribution and Thickness of Separated Boundary Layer

Typical velocity distributions of the normalized u-component on the suction surface of the natural wing and the cylinder-wake affected wing are selected and presented next to illustrate the detailed developments of the parallel velocity at different stages along the wing chord. The data are obtained by linear interpolation from the PIV measurements. The numerical values for the vertical axis in the following plots denote the quantity of $y\cos\alpha/c$, which symbolizes the distance away from the suction surface of the wing in the direction normal to the towing direction.

Figure 10 shows the distributions of the u-component along the $-\eta$ direction of the natural wing at various stages of x/c on the instant of $t^* = 4.333$. The Reynolds number and the angle of attack are 1200 and 15 deg, respectively. At each stage of x/c, the normalized u velocity profile, which is denoted by the symbol of an empty square □, remains almost constant in the region far away from the wing suction surface. For instance, $u/\bar{u}$ is a little more negative than -1 at $x/c = 0.125$ because the approaching freestream has sensed the existence of the leading-edge vortex pair as indicated in the plot of $t^* = 4.333$ in Fig. 3. It is accelerated to about -1.9, which is almost twice the approaching freestream velocity, at the stage of $x/c = 0.875$ because the space on the suction surface is "occupied" by the initial surface vortex and the trailing-edge vortex. The freestream is virtually blocked by the vortices so that the increase of velocity in the outer area velocity is expected. The symbol of the filled square ■ marked on each velocity profile denotes the location where the u velocity deviates by about 1% from the outer constant velocity area. The dashed line connecting all the filled squares can be taken as the border of the separated boundary layer, below which are the vortical flow structures. The thickness of the separated boundary layer increases with the increase of x/c and attains $y\cos\alpha/c \approx 0.425$ at half chord ($x/c = 0.5$), where the four-way saddle locates. From $x/c = 0.5$ to 0.625, a drastic increase in the thickness of the separated boundary layer is observed. This sudden increase is due to the existence of the initial surface vortex, as shown in the plot of $t^* = 4.333$ in Fig. 3. Below the border of the separated boundary layer, the instantaneous velocity profiles are subject to the influences of the dynamic vortical flow structures so that they look completely different from those usually seen in the time-averaged separated boundary layer. In the outer region of the separated boundary layer, the u velocity profile decreases from the large constant value to zero as denoted by a filled circle ●. The imaginary line connecting the symbol ● at all stages actually is very close to a line connecting the center points of the initial surface vortex and the leading-edge vortices in the plot of $t^* = 4.333$ in Fig. 3. Below the zero velocity line which connects the points denoted by ●, the flow is reversed towards the upstream direction so that the u velocity becomes positive. The filled triangular symbol ▲ denotes another change in the flow direction near the suction surface of the wing. Below the filled triangular symbol ▲, values of $u/\bar{u}$ in the region covered by the clockwise-rotating vortex of the leading-edge vortex pair and the trailing-edge vortex are negative because the flows in this region are heading towards the trailing-edge direction. At the stage $x/c = 0.625$, the symbol ▲ does not appear because a three-way saddle exists there on the suction surface to separate the near-surface flows between the clockwise-rotating vortex of the leading-edge vortex pair and the trailing-edge vortex. The three-way saddle on the suction surface can be clearly seen in the plot of $t^* = 4.333$ in Fig. 3. At the stage $x/c = 0.250$, the symbol ▲ does not appear because there is another three-way saddle located there on the suction surface to separate the flows between the clockwise-rotating and the counterclockwise-rotating vortices of the leading-edge vortex pair.

The instantaneous distributions of the u velocity along the chord length in the cylinder-wake affected case of cylinder angle $\theta = 60$ deg at $t^* = 2.288$ are shown in Fig. 11. The velocity profiles look quite different from those shown in Figs. 10 and 11. It is because the evolved flow pattern of the cylinder-wake affected wing in the plot of Fig. 7 at $t^* = 2.288$ is drastically different from those of Fig. 3 at $t^* = 4.333$ and Fig. 5 at $t^* = 3.396$. At $t^* = 2.288$ of Fig. 7, the trailing-edge vortex is about to leave the trailing edge of the wing for the downstream area. At $x/c \approx 0.25$ of Fig. 7 at $t^* = 2.288$, a three-way saddle exists on the suction surface of the wing, which separates the downstream-going gap flow and the reverse flow of the leading-edge vortex. Therefore, the symbol ● does not exist on the velocity profile at the stage $x/c = 0.25$ of Fig. 11. At all stages of $x/c > 0.25$ in Fig. 11, positive values of $u/\bar{u}$ appear below the symbol ●. In

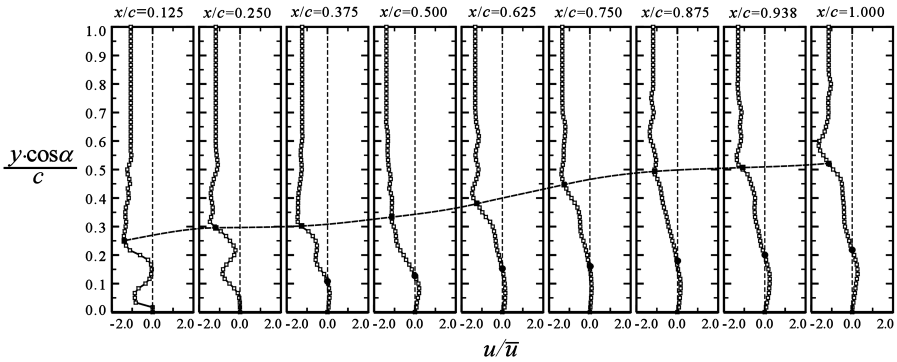

Fig. 11 Velocity distributions of normalized u-component on surface of cylinder-wake affected wing.

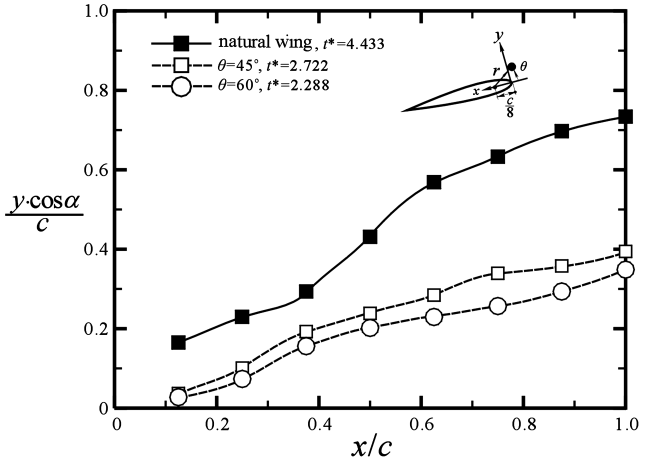

Fig. 12 Thickness of separated boundary layers on suction surface of natural and cylinder-wake affected wings.

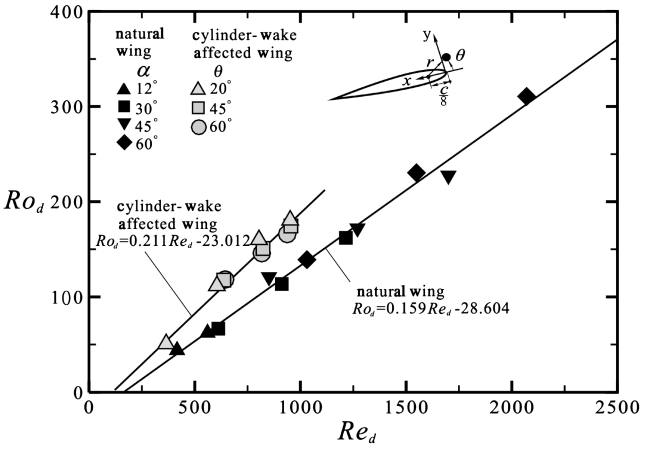

Fig. 13 Functional relationships between Roshko number and Reynolds number of vortex shedding.

other words, all the flows near the suction surface downstream the three-way saddle point are reversed toward the upstream direction. At the stages of $x/c = 0.125$ and 0.250, the near wake of the circular cylinder induces velocity deficit so that local regions of low velocities appear on the profiles within $y\cos\alpha/c \approx 0.1$–0.2 and 0.15–0.3, respectively.

The heights of the separated boundary layers measured from the wing chord at $t^* = 4.433$ are illustrated in Fig. 12. The phenomena are similar in all time stages. The thickness of separated boundary layer of the natural wing is much larger than those of the cylinder-wake affected wing. When the circular cylinder is placed at $\theta = 60$ deg, the effect of suppression on the thickness of the separated boundary layer is most apparent. The reduction in the thickness of the separated boundary layer and the change in the vortex evolution process induced by the installation of the circular cylinder should induce appreciable alterations in the drag and lift of the wing.

Vortex Shedding Frequency

As described in the preceding sections, the alternative releases of the surface vortex and the trailing-edge vortex from the suction surface of the wing model cause periodic instabilities in the wake, which are conventionally called the vortex shedding [17]. The vortex shedding frequency can be measured by counting the vortex release rate by observing the recorded flow visualization streak pictures. It is conventionally correlated by the Roshko number $Ro_d \equiv fd^2/\nu$ and the Reynolds number $Re_d \equiv \bar{u}d/\nu$, based on the length scale and the kinetic viscosity of water. The physical width is the length of the wing section projection on the cross-stream plane. The Roshko number has been adopted by many investigators to correlate the instability frequency of the periodic wakes [18–21]. It is an indication of the viscous effect on the instability frequency because no inertial force is included. By applying the similarity theory and dimensional analysis to the asymptotic ranges of Reynolds number, Huang and Lee [22] concluded that the Roshko number is expected to remain constant if the Reynolds number is small enough in the viscous-effect-dominated regime, probably in the order of one or 10. In the regime of the Reynolds number larger than about $400 \sim 500$, the inertial effect dominates the hydrodynamic stability so that the Roshko number should increase linearly with the increase of Reynolds number.

Figure 13 shows the results of the correlation between the Roshko number and the Reynolds number. The data of the natural wing are obtained from Huang et al. [6]. The Roshko numbers of both the natural wing and the cylinder-wake affected wing increase almost linearly with the increase of the Reynolds number. The Roshko number of the cylinder-wake affected wing is generally larger than that of the natural wing in both the magnitude and the increase rate. Apparently, the vortex shedding in the wake at the present Reynolds numbers is beyond the viscosity-dominated regime. The correlated equations are provided below for convenience of use:

$$Ro_d = 0.159Re_d - 28.604 \qquad \text{for natural wing} \tag{1}$$

and

$$Ro_d = 0.211Re_d - 23.012 \qquad \text{for cylinder-wake affected wing} \tag{2}$$

Another frequently used nondimensional group to correlate dynamic data in the wake is the Strouhal number, which is defined by $Sr_d \equiv fd/\bar{u}$. The Strouhal number is a parameter representing the inertial effect on the instability frequency because no viscous term is included. The Strouhal number, Roshko number, and Reynolds number can be interrelated by the following equation:

$$Sr_d = \frac{fd}{\bar{u}} = \left(\frac{fd^2}{\upsilon}\right) \Big/ \left(\frac{\bar{u}d}{\upsilon}\right) = \frac{Ro_d}{Re_d} \tag{3}$$

Therefore, Eqs. (1) and (2) can be converted into the relationships between the Strouhal number and the Reynolds number by dividing through with Re_d. The results are

$$Sr_d = 0.159 - 28.604/Re_d \qquad \text{for natural wing} \tag{4}$$

and

$$Sr_d = 0.211 - 23.012/Re_d \qquad \text{for cylinder-wake affected wing} \tag{5}$$

The Strouhal number data and the Eqs. (4) and (5) are plotted in Fig. 14. For the natural wing, the Strouhal number increases with the Reynolds number when $Re_d < 1500$, then approaches almost constant when the Reynolds number is large. The ultimate Strouhal number would attain about a constant 0.16 in the inertial dominated

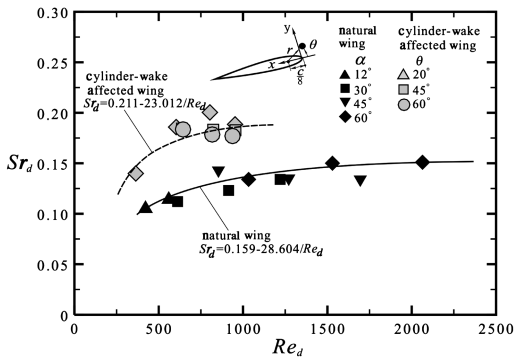

Fig. 14 Functional relationships between Strouhal number and Reynolds number of vortex shedding.

regime as predicted by Eq. (4). Apparently, the present experiment is not within the limiting regime where the viscous or inertial effect totally dominates. For the cylinder-wake affected wing, the Strouhal number increases with the Reynolds number when $Re_d < 600$, then approaches almost constant when the Reynolds number is large. The ultimate Strouhal number would attain about a constant 0.21 in the inertial dominated regime as predicted by Eq. (5). The extreme value 0.21 as the Reynolds number approaches infinity of the cylinder-wake affected wing happens to be about the same as that of a circular cylinder [18]. It is about 33% higher than that of the natural wing.

Conclusions

The vortical flow structures in the separated boundary layer on the suction surface of the NACA 0012 natural wing present complex temporal and spatial evolution process. The vortex shedding in the wing wake is the result of alternative release of the surface vortex and the trailing-edge vortex, which is temporally formed during the vortex evolution process which has occurred on the suction surface of the wing. If a circular cylinder of small diameter is placed around the near-nose area above the wing surface at a proper distance, the evolution process of the vortical flow structure on the wing surface, the thickness of the separated boundary layer, and the vortex release rate to the wake are significantly altered. The alterations may be attributed to the formation of a flow curtain which is induced by the jetlike stream going through the gap between the cylinder and the wing surface. The flow curtain applies large shear on the separated boundary layer and suppresses the growth of it. Therefore, the thickness of the separated boundary layer is drastically reduced by more than 50% and the vortex evolution process is modulated to a different mode. Because the shear applied on the separated boundary layer is increased, the evolution process of the vortical flow structures is accelerated. Therefore the vortex shedding frequency of the cylinder-wake affected wing is increased. The extreme value of the Strouhal number of the cylinder-wake affected wing can be increased to a value about 33% higher than that of the natural wing.

References

[1] Arena, A. V., and Mueller, T. J., "Laminar Separation, Transition, and Turbulent Reattachment near the Leading Edge of Airfoils," *AIAA Journal*, Vol. 18, No. 7, 1980, pp. 747–753.

[2] Lissaman, P. B. S., "Low Reynolds Number Airfoils," *Annual Review of Fluid Mechanics*, Vol. 15, 1983, pp. 223–239.

[3] Ohmi, K., Coutanceau, M., Daube, O., and Loc, T. P., "Further Experiments on Vortex Formation Around an Oscillating and Translating Airfoil at Large Incidences," *Journal of Fluid Mechanics*, Vol. 225, April 1991, pp. 607–630.

[4] Coutanceau, M., and Pineau, G., "Some Typical Mechanisms in the Early Phase of the Vortex-Shedding Process from Particle-Streak Visualization," *Atlas of Visualization 3*, edited by Nakayama, Y., and Tanida, Y., CRC Press, Boca Raton, FL, 1997, pp. 43–68.

[5] Nair, M. T., and Sengupta, T. K., "Unsteady Flow Past Elliptic Cylinders," *Journal of Fluids and Structures*, Vol. 11, No. 6, 1997, pp. 555–595.

[6] Huang, R. F., Wu, J. Y., Jeng, J. H., and Chen, R. C., "Surface Flow and Vortex Shedding of an Impulsively Started Wing," *Journal of Fluid Mechanics*, Vol. 441, 2001, pp. 265–292.

[7] Gad-el-Hak, M., "Control of Low-Speed Airfoil Aerodynamics," *AIAA Journal*, Vol. 28, No. 11, 1990, pp. 1537–1552.

[8] Gad-el-Hak, M., "Introduction to Flow Control," *Flow Control Fundamentals and Practices*, edited by Gad-el-Hak, M., Pollard, A., and Bonnet, J.-P., Springer–Verlag, Berlin, 1998, pp. 1–153.

[9] Strykowski, P. J., and Sreenivasan, K. R., "On the Formation and Suppression of Vortex Shedding at Low Reynolds Numbers," *Journal of Fluid Mechanics*, Vol. 218, 1990, pp. 71–107.

[10] Abbot, I. H., and Von Doenhoff, A. E., *Theory of Wing Section*, Dover, New York, 1959, pp. 113–115.

[11] Richard, C. F., and John, H. S., *Fundamentals of Air Pollution Engineering*, Prentice–Hall, Upper Saddle River, NJ, 1988, pp. 290–357.

[12] Kean, R. D., and Adrian, R. J., "Theory of Cross-Correlation Analysis of PIV Images," *Applied Scientific Research*, Vol. 49, No. 3, 1992, pp. 191–215.

[13] Kean, R. D., and Adrian, R. J., "Optimization of Particle Image Velocimeters Part 1: Double Pulsed Systems," *Measurement Science and Technology*, Vol. 1, No. 11, 1990, pp. 1202–1215.

[14] Abernethy, R. B., Benedict, R. P., and Doedell, R. B., "ASME Measurement Uncertainty," *Journal of Fluids Engineering*, Vol. 107, No. 2, 1985, pp. 161–164.

[15] Perry, A. E., and Fairlie, B. D., "Critical Points in Flow Patterns," *Advances in Geophysics*, Vol. 18, 1974, pp. 299–315.

[16] Roshko, A., "On the Development of Turbulent Wakes from Vortex Streets," NACA, Rept. 1191, 1954.

[17] Tritton, D. J., *Physical Fluid Dynamics*, Oxford Univ. Press, Oxford, England, U.K., 1988, pp. 243–277.

[18] Roshko, A., "On the Wake and Drag of Bluff Bodies," *Journal of Aerospace Science and Technology*, Vol. 22, Feb. 1955, pp. 124–135.

[19] Simmons, J. E. L., "Similarities Between Two-Dimensional and Axisymmetric Vortex Wakes," *Aeronautical Quarterly*, Vol. 26, Feb. 1977, pp. 15–20.

[20] Levi, E., "Universal Strouhal Law," *Journal of Engineering Mechanics*, Vol. 109, No. 3, 1983, pp. 718–727.

[21] Berger, E., and Wille, R., "Periodic Flow Phenomena," *Annual Review of Fluid Mechanics*, Vol. 4, 1972, pp. 313–340.

[22] Huang, R. F., and Lee, H. W., "Turbulence Effect on Frequency Characteristics of Unsteady Motions in Wake of Wing," *AIAA Journal*, Vol. 38, No. 1, Jan. 2000, pp. 87–94.

R. Lucht
Associate Editor